

Supplementary Informations:

Hybrid Pyrophototronic Nanogenerator (HPyNG) for Ultra-low Light Detection

Santanu Podder^{†,a,b}, Jyotisman Bora^{†,a}, Khomdram Bijoykumar Singh^{a,c}, Deepshikha Gogoi^{a,d}, Bablu Basumatary^{a,e}, Arup R. Pal^{a,c}*

† Contributed Equally

^a Plasma Nanotechnology Laboratory, Physical Sciences Division, Institute of Advanced Study in Science and Technology, Paschim Boragaon, Garchuk, Guwahati -781035, India

^b Centre for Nanotechnology, IIT Guwahati, India-781039

^c Academy of Scientific and Innovative Research (AcSIR), Ghaziabad – 201002, India

^d Department of Physics, Abhayapuri College, Abhayapuri, Assam, India-783384

^e Department of Physics, Dimoria College, Khetri, Kamrup, Assam, India-782403

**Corresponding Author:*

E-mail: arpal@iasst.gov.in, Tel.: +91 361 2912073. Fax: +91 361 2279909

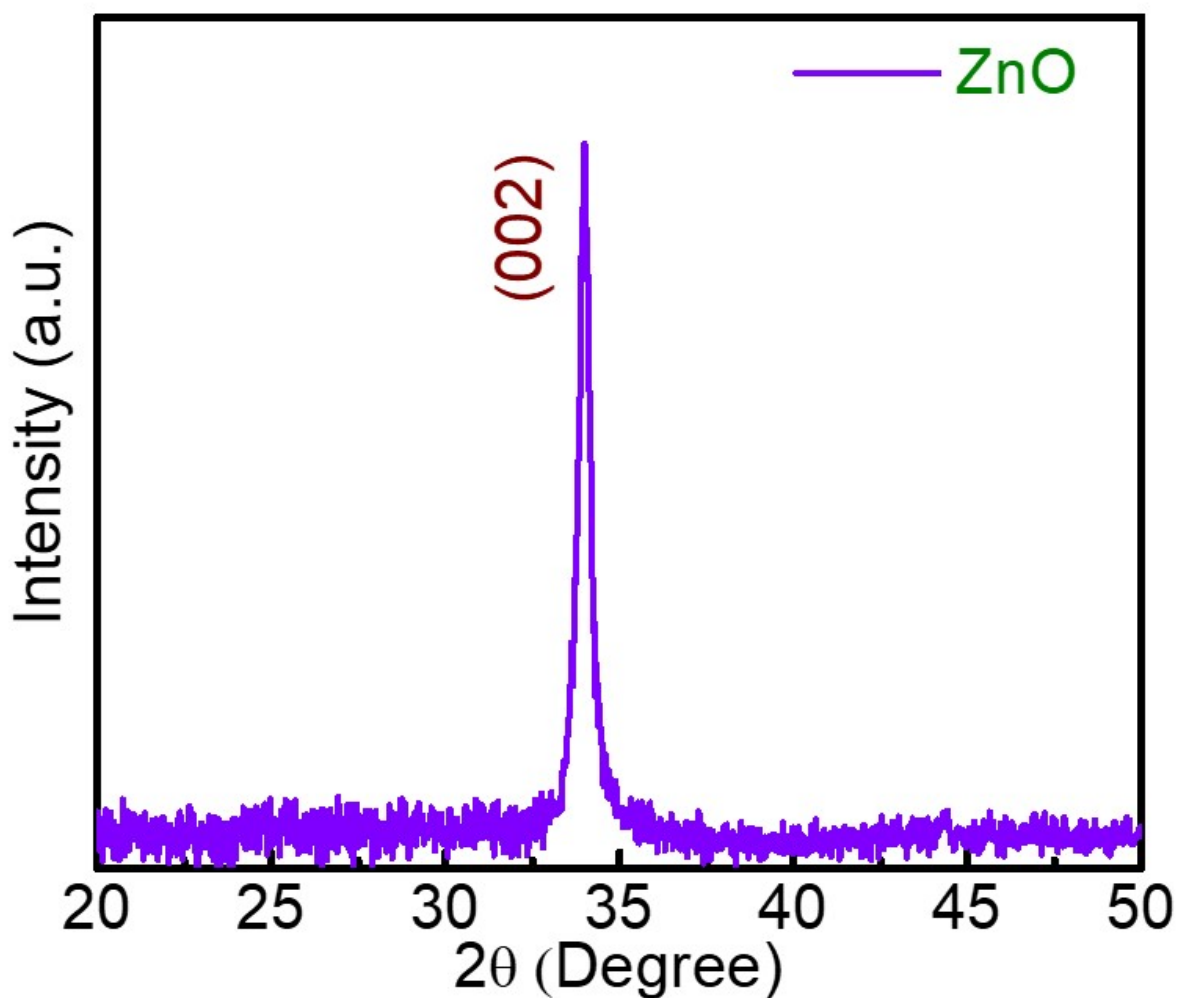


Figure S1 XRD pattern of the synthesised ZnO thin film

X-Ray Diffraction spectrum of the synthesized ZnO thin film is recorded with a BRUKER D8 advanced spectrometer and the pattern is shown in Figure S1. The pattern shows a very strong diffraction peak at 34° which corresponds to the (002) crystal plane of the wurtzite phase of zinc oxide. This crystalline phase of ZnO is non-centrosymmetric in nature and thereby shows pyroelectric effect. The strong XRD peak also reveals the formation of highly crystalline structure which strengthens the generated pyroelectric current within this material.¹

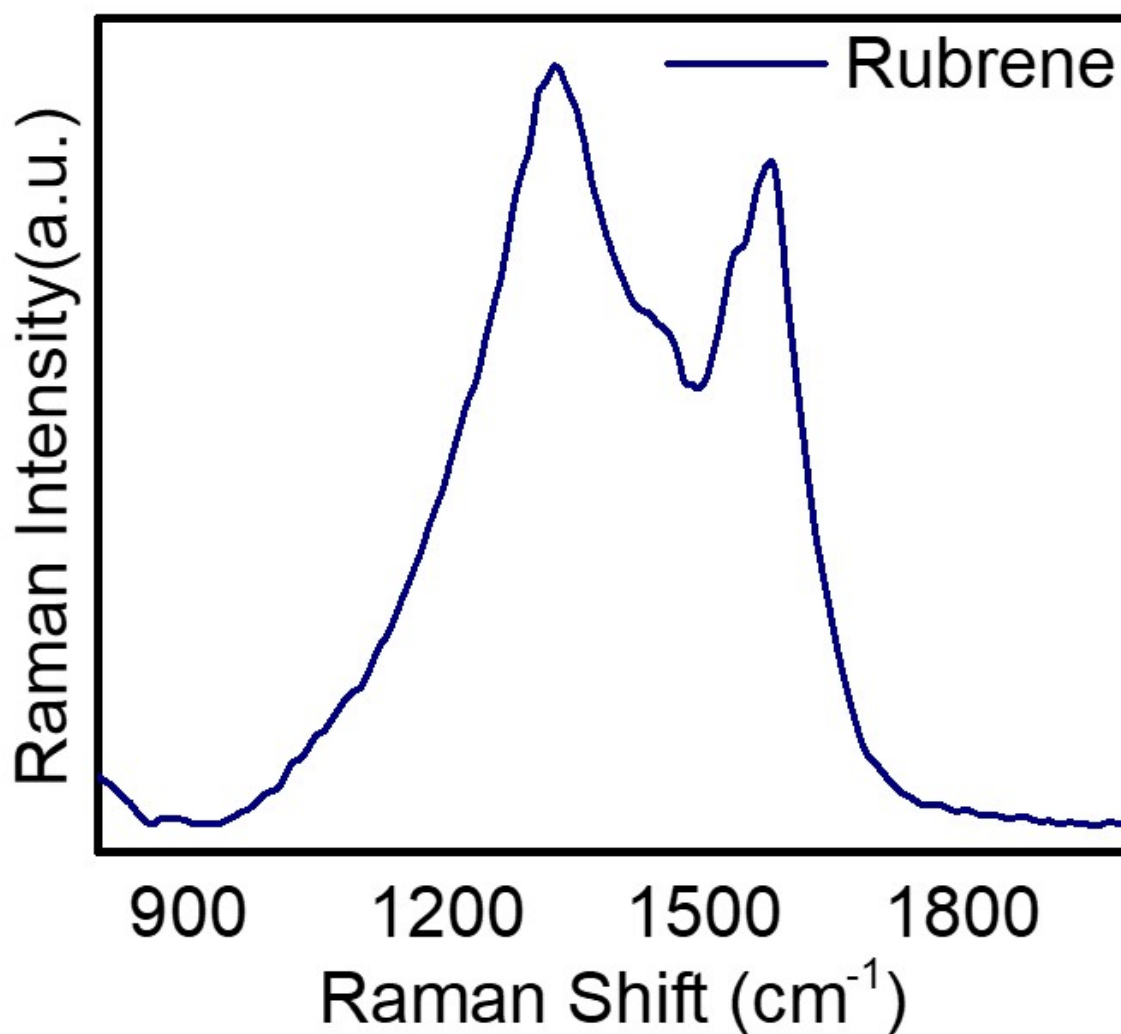


Figure S2 Raman spectrum of the PPA Rubrene composite

Raman spectroscopy is a non-destructive material characterization technique to confirm the chemical and molecular structure of the as synthesized sample. Raman spectra of the sample is recorded with a commercial spectrometer (Horiba JobinVyon, model LabRam HR Evolution) using an Ar-ion laser with an excitation wavelength of 514 nm (2.41 eV). Figure S2 shows the Raman spectra of the synthesized PPA-Rubrene composite. The strong peak appears at 1315 cm⁻¹, 1418 cm⁻¹ and 1591 cm⁻¹ indicates the vibrations of the cyclic aromatic

compounds of phenyl and tetracene units present in rubrene. These peaks confirms the crystalline nature of the rubrene and it is consistent with the available literature reports.²³

Table S1: Summary of the kinetic parameters obtained from the fitting of the TRPL spectra of ZnO and ZnO/Rubrene combination by using tri exponential decay functions.

Material	τ_1 [ns]	B_1	τ_2 [ns]	B_2	τ_3 [ns]	B_3	$\langle \tau \rangle$ [ns]	τ_{CT} [ns]	η [%]
ZnO	0.234717	0.0308	0.021817	2.550225	5.499721	0.017218	3.32	4.28	43.69
ZnO/Ru brene	1.024903	0.00144	5.240613	0.004077	0.055044	0.707649	1.87		

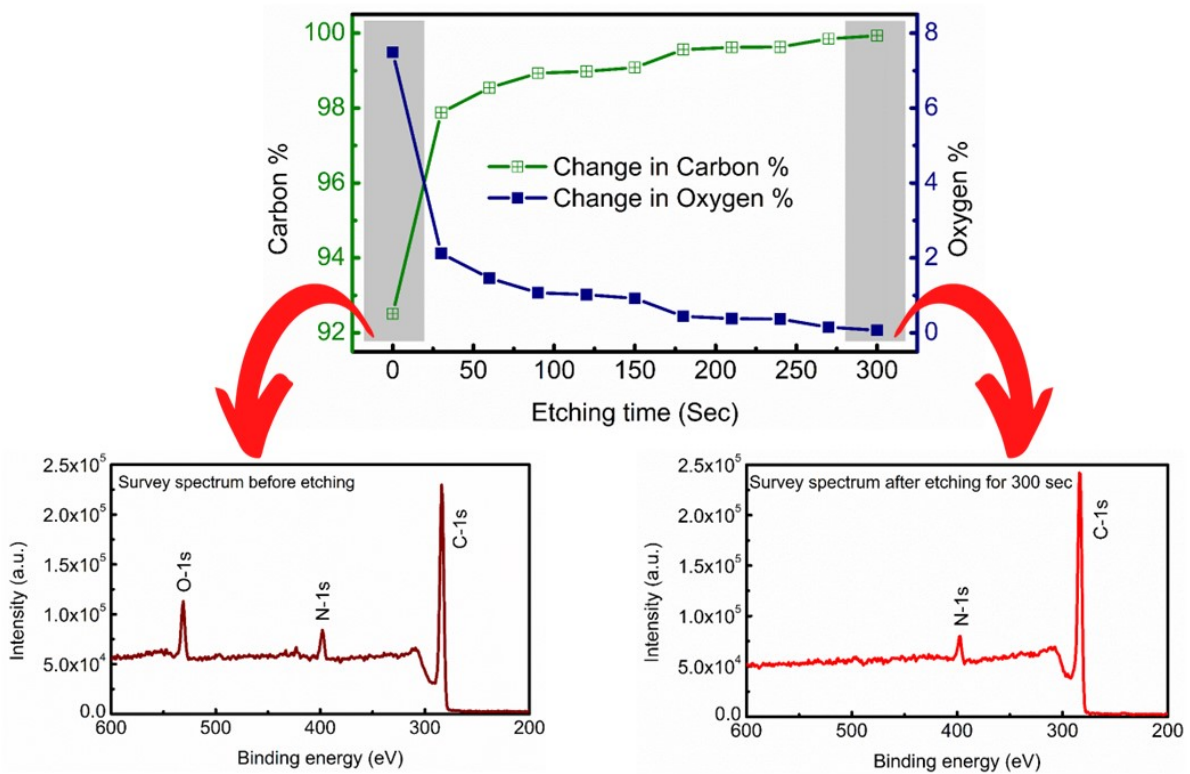


Figure S3 XPS depth profile of the Rubrene sample along with the survey spectrum without etching and with etching for 300 sec.

Figure S3 shows the XPS depth profiling of the synthesised PPA rubrene composite. The study is carried out with help of a ESCALAB Xi+ instrument (Thermo Fisher). The study reveals that on top of the surface of the sample, the atomic percentage of oxygen is high and as we are going towards the bulk of the sample with the help of etching, oxygen atomic percentage reduces to almost negligible stage. The study reveals the presence of a surface oxidized layer which is responsible for the pyroelectric phenomena in crystalline rubrene. The initial (without etching) and final (with etching for 300 sec) survey spectra are also given for better understanding.

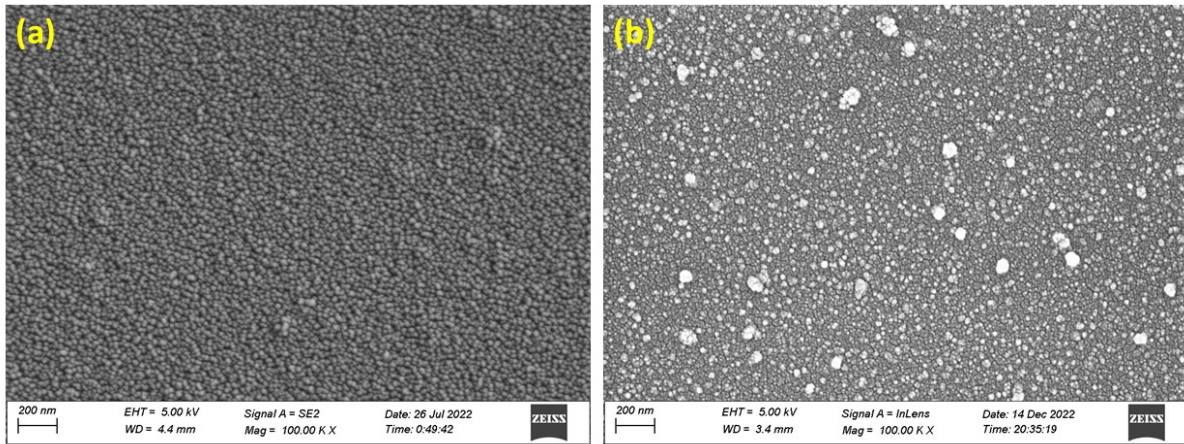


Figure S4 FESEM image of (a) ZnO and (b) PPA-Rubrene composite

The surface morphology of the synthesized samples are studied using Field Emission Scanning Electron Microscopy (FESEM). The study is done with the help of a SIGMA VP ZEISS instrument. The morphology of ZnO (Figure S4 (a)) reveals the formation of a very smooth thin film which is responsible for nullifying the leakage current in the fabricated device. Figure S4 (b) shows the FESEM image of PPA Rubrene composite which confirms the growth of Rubrene crystallites within the PPA matrix.

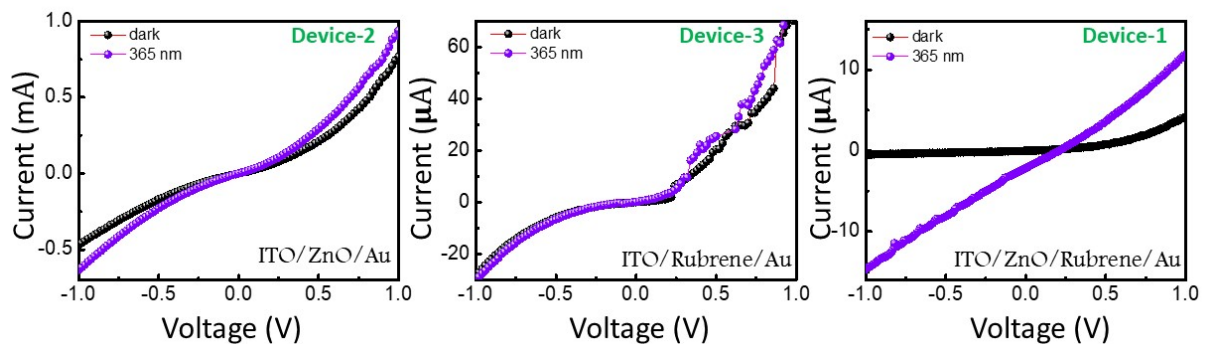


Figure S5 I-V characteristic curves of the fabricated devices.

Figure S5 shows the I-V characteristics curves of the fabricated devices recorded with the help of a Keithley 2634B Source meter. The study shows the the combination of ZnO and Rubrene generates much higher photocurrent and photovoltage as compared to the devices made with individual materials.

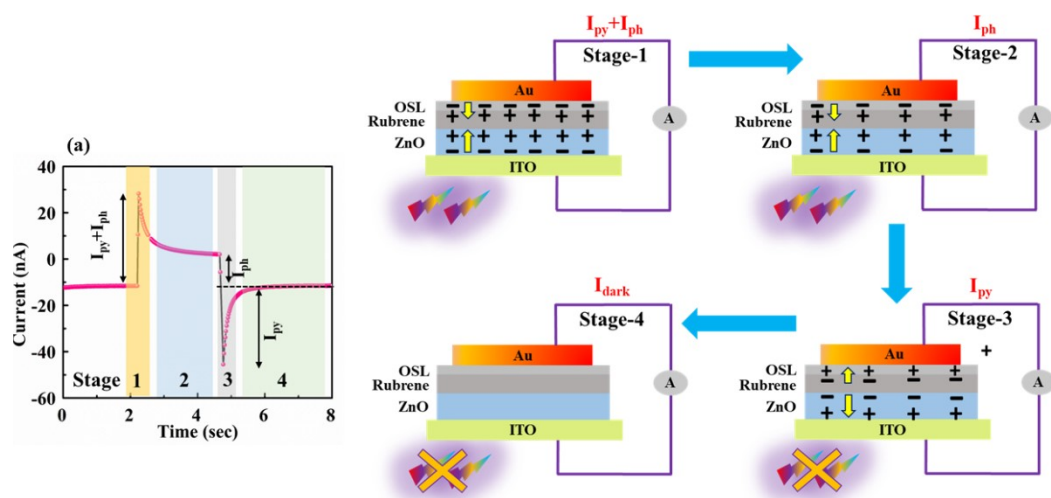


Figure S6 Schematic representation of the 4 stage current generation process in Device-1 as a result of combined pyro-photo effect.

There are four stages of current generation in a single on-off cycle. Figure S6 provides a systematic explanation of the mechanism underlying each level. The total current generated in the device upon illumination, as observed in Stage-1, is a combination of both photocurrent and pyroelectric current. ($I_{py}+I_{ph}$). The photocurrent is generated due to the creation of charge carriers in the device when exposed to UV light. The pyroelectric current in this stage is contributed by both ZnO and Rubrene by two different mechanism as mentioned in the main text. In ZnO, the light-induced transient heating causes an atomic rearrangement in the crystal, which produces electric polarization in the c-axis direction (upward). Whereas the surface

polarization is responsible for the origin of pyroelectricity in Rubrene film. The electronegative nature of oxide surface layer (OSL) produces negative charges and induces positive charges toward the interface of the crystalline Rubrene film. This process results in the surface polarization directed downward. The opposite directional polarization of both the materials diminishes the overall pyroelectric current in stage-1. In the stage-2, the effect of transient heat disappears and as a result of that, pyroelectric current vanishes. In this stage, the current flowing in the device is solely due to the photocurrent (I_{ph}). After switching off the UV light, transient heat fluctuation occurs further. However, this time, the polarization reverses direction, and the current flowing through the device is solely due to the pyroelectric effect (I_{py}). In Stage-4, both transient heating and pyroelectric polarization disappear, leaving only the dark current flowing in the device.

FDTD Simulation Study:

Using commercially available software, Ansys Lumerical, which employed FDTD (Finite-difference time domain) method, an optical cross-section of the synthesized materials and electric field distribution of the fabricated devices are studied. The simulation is executed by maneuvering the refractive index values (n and k) of ZnO and Rubrene, extracted from Spectroscopic Ellipsometry (SE) analysis, while the standard dielectric constant values for ITO and Au films are sourced from the Lumerical Database.^{4,5} Proper boundary conditions, such as symmetric, antisymmetric, and PML (Perfectly matched layer), for the FDTD region are defined. The surrounding medium refractive index is set to 1 for air. A TFSF (Total Field Scatter Field) power source is employed to simulate s and p polarization differently from

wavelength ranging from 300 nm to 800 nm. The light is illuminated from the ITO side to the forward direction along the positive z-axis. Frequency domain field monitors are used to determine the spatial distribution of electric fields in all three different device configurations. A mesh properly surrounds the nanostructure materials with override meshing dimensions dx, dy, and dz set to 0.5 nm. The nanostructure models are set as follows: the thickness of ZnO, Rubrene, ITO, and Au film is 60 nm, 100 nm, 100 nm, and 70 nm, respectively.

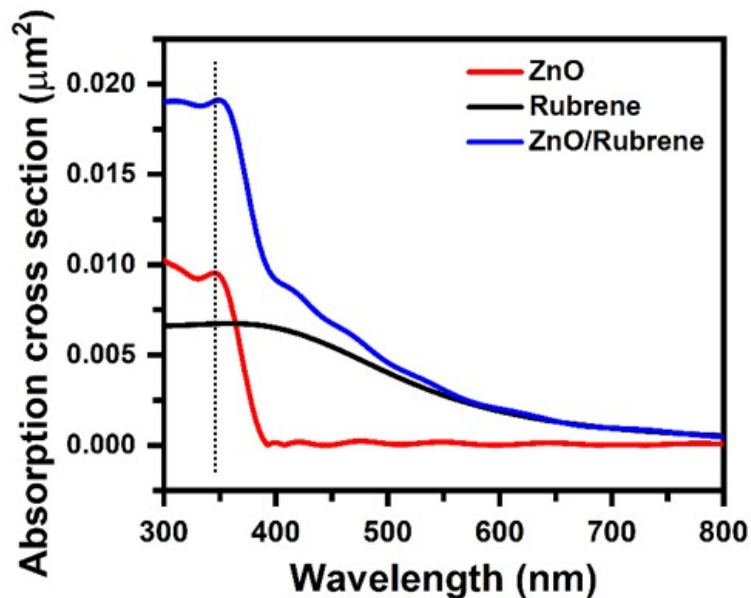


Figure S7 Simulated absorption spectra of the photoactive materials of the fabricated device.

Absorption cross-sections of the nanostructure materials are carried out without ITO and Au film in the s and p-polarized states. No significant changes in results are observed with s and p polarization, so only results for one particular polarization (i.e., p-polarized) are shown here. The simulated absorption cross-section of ZnO is represented in Figure S7 by a red line, which shows the absorption in the UV region with a maxima peak at 350 nm. The simulated

absorption cross section of Rubrene is also shown by a black line, which is consistent with the experimental UV-Vis spectrum. A slight red-shift in the absorption cross-section peak of the combined ZnO and Rubrene nanostructure system is observed, resulting from the effective interaction between ZnO and Rubrene. The absorption cross-section of the combined system is significantly large in the UV region, indicating a favourable condition for the conversion of UV light into photocurrent.

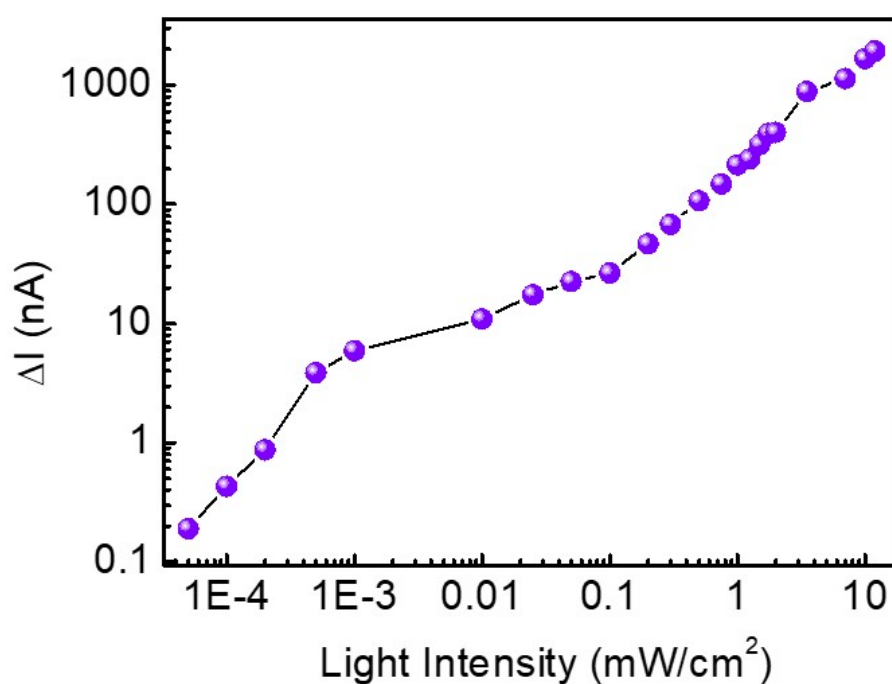


Figure S8 Generation of photocurrent a function of light intensity presented in logarithmic scale.

Figure S8 illustrates the photocurrent generation as a function of light intensity, plotted on a logarithmic scale. The linear relationship observed between these two quantities suggests that the device maintains a constant photoresponsivity across different intensity levels.

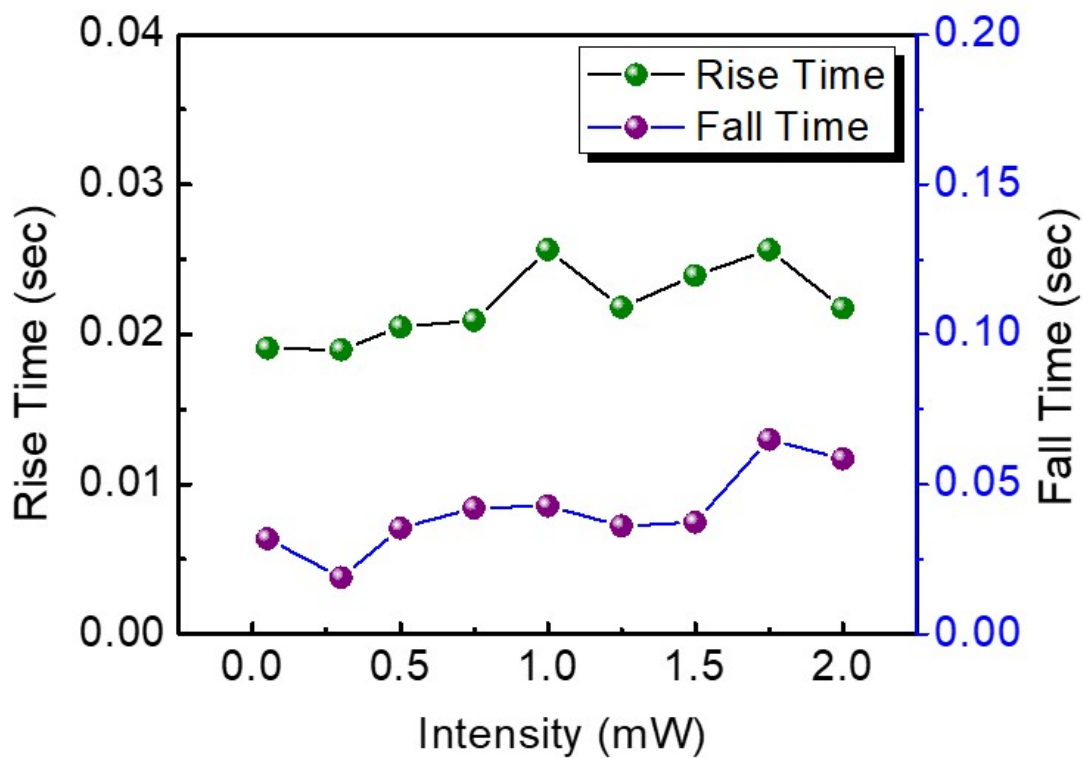


Figure S9 Rise and Fall times of the device as a function of light intensity

The response times, i.e., the rise time and fall time of the device, are calculated as a function of light intensity and presented in Figure S9. It is observed that the response times do not vary significantly with light intensity. The fastest response time of the device is determined to be 18 ms.

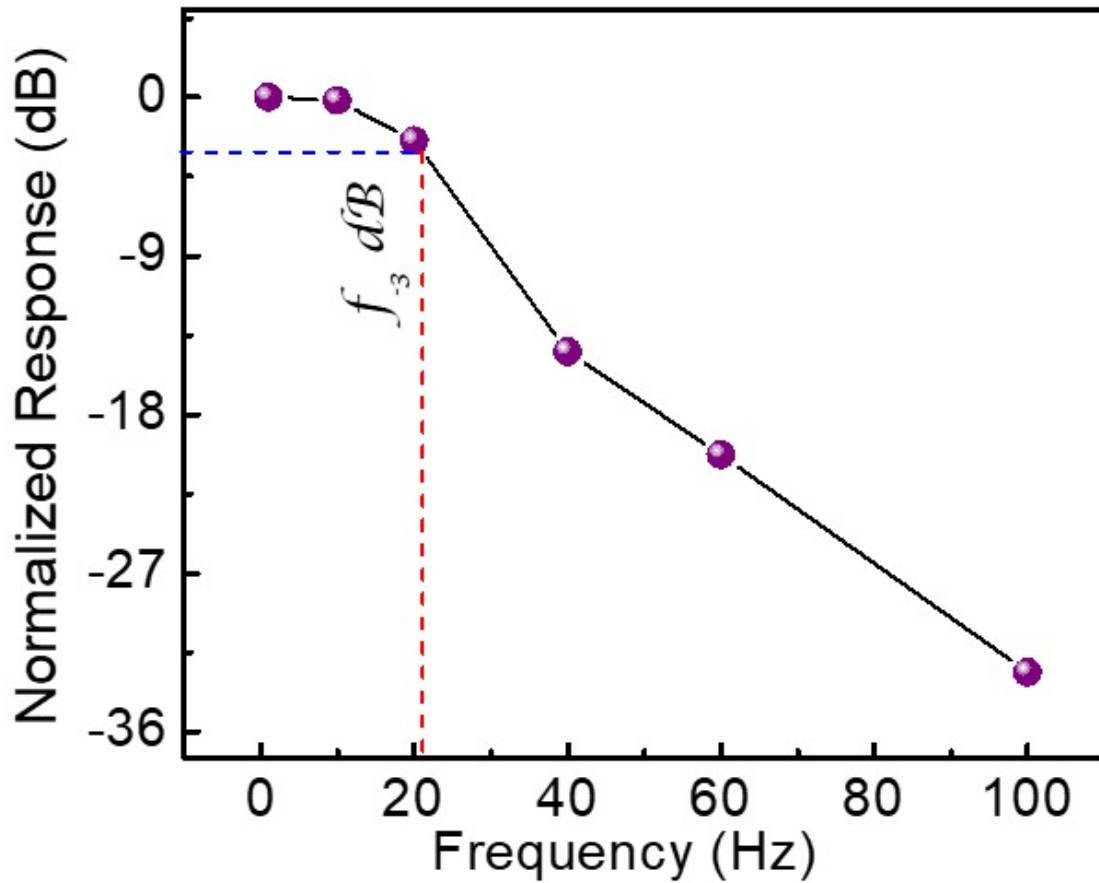


Figure S10 Normalized frequency response of the device for calculating 3 dB frequency

The normalized response of the fabricated device is calculated by varying the illuminated light frequency. The recorded data is shown in Figure S10. This study is very important to check the high-speed applications of the devices. From that study the 3 dB frequency value is calculated and it is found out to be 10 Hz. The 3 dB frequency is basically that frequency at which the response of the device attenuated by 3 dB or 70.8% of its initial output.⁶

To compare the performance of the fabricated device with other existing devices reported in the literature, a comparative study has been conducted, and the results are

summarized in Table S2. This study clearly highlights the device's capability to compete with its counterparts.

Table S2: Performance Comparison of Reported ZnO-Based Self-Powered UV Detectors with Other Published Devices:

Device Structure	Photoresponsivity (R_i) [mA W^{-1}]	Detectivity (D^*) [Jones]	Response Time [ms]	Ref.
Cl-ZnO/PEDOT:PSS	2.33	3.5×10^9	28	7
ZnO/PEDOT:PSS	3.5	7.5×10^9	5.8	8
H:VZnO NFs/PEDOT:PSS	2.65	5.25×10^{10}	23	9
ZnO/CuI/Au	61.5	1.7×10^{10}	410	10
ZnO/Au/Al ₂ O ₃	6.8	1.7×10^9	160	11
ZnO@CdS/PEDOS	7.68	5.62×10^{11}	190	12
ZnO:Ni (5%) NRs	0.049	1.132×10^8	10	13
3D ZnO/CFP composites	31.76	3.06×10^{12}	76.51	14
annealed ZnO/SrTiO ₃	0.7	4.5×10^{12}	0.035	15
ZnO/Rubrene	15	4×10^9	18	This Work

References:

- 1 S. Podder, B. Basumatary, D. Gogoi, J. Bora and A. R. Pal, *Appl. Surf. Sci.*, 2021, **537**, 147893.

- 2 K. P. Dhakal, J. Joo and J. Kim, *Curr. Appl. Phys.*, 2022, **39**, 304–310.
- 3 S. Biswasi, D. Gogoi and A. R. Pal, *Appl. Surf. Sci.*, 2022, **599**, 153883.
- 4 P. B. Johnson, R. W. Christy, *Phys. Rev. B*, 1972, **6**, 4370–4379.
- 5 T. A. F. König, P. A. Ledin, J. Kerszulis, M. A. Mahmoud, M. A. El-Sayed, J. R. Reynolds and V. V. Tsukruk, *ACS Nano*, 2014, **8**, 6182–6192.
- 6 R. Li, S. Bai, Z. Jia, X. Chen, Y. Liu and Q. Lin, *ACS Photonics*, 2024, **11**, 2521–2527.
- 7 B. Deka Boruah, S. Naidu Majji, S. Nandi and A. Misra, *Nanoscale*, 2018, **10**, 3451–3459.
- 8 W. Peng, X. Wang, R. Yu, Y. Dai, H. Zou, A. C. Wang, Y. He and Z. L. Wang, *Adv. Mater.*, 2017, **29**, 1606698.
- 9 B. Deka Boruah and A. Misra, *ACS Appl. Mater. Interfaces*, 2016, **8**, 18182–18188.
- 10 X. J. Fa Cao, Ling Jin, Yong Wu, *J. Alloys Compd.*, 2005, **859**, 158383.
- 11 F. Cao and X. Ji, *J. Mater. Sci. Mater. Electron.*, 2020, **31**, 2657–2665.
- 12 A. Kadir, T. Abdiryim, X. Liu, R. Jamal and X. Tang, *Sensors Actuators A. Phys.*, 2024, **377**, 115698.
- 13 A. Bora, J. George, Y. Sivalingam, S. Velappa Jayaraman, G. Magna, M. S. R. N. Kiran, L. Vesce, R. Paolesse and C. Di Natale, *ACS Appl. Nano Mater.*, 2024, **7**, 9324–9336.

- 14 F. Xu, W. Yan, D. Pang, B. Ren, Q. Tang, X. Wang, G. Tan, H. Li, Y. Xiong, Y. Tang, L. Ye, C. Kong and H. Zhang, *Opt. Mater. (Amst)*., 2024, **150**, 115185.
- 15 L. Cong, Y. Han, H. Zhao, C. Gao, W. Zhang, S. Zhang and H. Wang, *J. Mater. Chem. C*, 2024, **12**, 6911–6919.